Title

Tuning Internal Strain in Metal–Organic Frameworks via Vapor Phase Infiltration for CO2 Reduction

Journal

Angewandte Chemie International Edition, 59(11)

ISSN

1433-7851

Authors

Yang, Fan
Hu, Wenhui
Yang, Chongqing
et al.

Publication Date

2020-03-09

DOI

10.1002/anie.202000022

Peer reviewed

Tuning Internal Strain in Metal–Organic Frameworks via Vapor Phase Infiltration for CO_2 Reduction

Fan Yang, Wenhui Hu, Chongqing Yang, Margaret Patrick, Andrew L. Cooksy, Jian Zhang, Jeffery A. Aguiar, Chengcheng Fang, Yinghua Zhou, Ying Shirley Meng, Jier Huang,* and Jing Gu**

Abstract: *A gas-phase approach to form Zn coordination sites on metal–organic frameworks (MOFs) by vapor-phase infiltration (VPI) was developed. Compared to Zn sites synthesized by the solution-phase method, VPI samples revealed approximately 2.8% internal strain. Faradaic efficiency towards conversion of CO_2 to CO was enhanced by up to a factor of four, and the initial potential was positively shifted by 200–300 mV. Using element-specific X-ray absorption spectroscopy, the local coordination environment of the Zn center was determined to have square-pyramidal geometry with four Zn–N bonds in the equatorial plane and one Zn-OH_2 bond in the axial plane. The fine-tuned internal strain was further supported by monitoring changes in XRD and UV/Visible absorption spectra across a range of infiltration cycles. The ability to use internal strain to increase catalytic activity of MOFs suggests that applying this strategy will enhance intrinsic catalytic capabilities of a variety of porous materials.*

Introduction

Strain is one of the most common physical phenomena in solid-state materials, and is fundamentally important for controlling the reactivity of catalysts.[1] Progress in nanotechnology and advanced microscopic techniques has recently enabled the study of strain-tuned catalytic processes.[2] To date, numerous approaches have been developed to induce surface strains. Examples include introducing a subsurface inert gas by low-energy inert ion bombardment,[3] physical stretching of the support substrate,[4] and extracting and intercalating ions in layered structures to induce crystal structure changes.[5] However, most strain-related catalysis previously reported involves heterogeneous catalysts.[2b] For homogeneous-like metal–ligand catalytic systems, the strain effect has rarely been discussed. Inherent difficulty in investigating these systems originates from the lack of effective methods to generate distortion on individual metal active sites. Unlike earlier methods, this work employs vapor phase infiltration (VPI) to synthesize and induce strain in homogeneous-like metal–ligand active centers on metal–organic frameworks (MOFs).

MOFs are a class of 3D crystalline mesoporous materials constructed by interconnecting metal cluster nodes with multi-dentate organic linkers. Their highly crystalline nature and adjustable pore size provides a strong basis for understanding the distribution of metal active sites.[6] The porous structure facilitates diffusion of substances through its confined channels, making MOFs an ideal platform for inserting and evaluating metal catalytic centers. Those active sites can be introduced into MOFs by incorporating metals onto either metal nodes or bridging ligands.[7] Specifically, metal–ligand bridging units are able to maintain properties similar to their homogeneous analogues. Past reports have investigated the elastic properties of single-crystal MOFs by analyzing the effect of pressure on the system. Results showed that high pressure condition (0–9.9 GPa) can cause the MOF unit cell volume to decrease by over 27%, while leaving its original structure intact.[8] To date, limited progress has been made to correlate the strain effect and catalytic performance of MOF catalysis. Only recently, Liu et al. reported a bifunctional oxygen electrocatalyst NiFe MOF in which strains were instigated by photo-induced internal ligand decomposition.[2a] In this work, we demonstrate a more general VPI method which can generate finely controlled internal strain in MOF structures.

[*] Dr. F. Yang, M. Patrick, Prof. A. L. Cooksy, Prof. Y. Zhou, Prof. J. Gu
Department of Chemistry and Biochemistry, San Diego State University
5500 Campanile Drive, San Diego (USA)
E-mail: jgu@sdsu.edu

W. Hu, Prof. J. Huang
Department of Chemistry, Marquette University
Milwaukee, WI 53201 (USA)
E-mail: jier.huang@marquette.edu

Dr. C. Yang, Dr. J. Zhang
The Molecular Foundry, Lawrence Berkeley National Laboratory
Berkeley, CA 94720 (USA)

Dr. J. A. Aguiar
Nuclear Materials Department, Idaho National Laboratory
2525 Fremont Avenue, Idaho Falls, ID 83415 (USA)

Dr. C. Fang, Prof. Y. S. Meng
Materials Science and Engineering Program
University of California San Diego
La Jolla, CA 92093 (USA)

Prof. Y. Zhou
The Key Laboratory of Functional Molecular Solids, Ministry of Education, Anhui Laboratory of Molecule-Based Materials, College of Chemistry and Materials Science, Anhui Normal University
Wuhu, 241000 (China)
E-mail: yhzhou@ahnu.edu.cn

Atomic layer deposition (ALD) is a well-known thin film technique widely employed in surface engineering applications.[9] The chemical nature of ALD provides uniform layer formation across substrate surfaces that would normally exhibit nonlinear depth profiles. In this method, porous substrates allow gas phase precursors to penetrate and diffuse through their nanoporous structures, allowing the precursors to grow within the subsurface. This is known as the VPI process.[10] In some cases, when the porous structure contains coordination ligands, the metal precursor can bond with the ligands and form a metal–ligand coordination.[11] VPI has proven successful in distributing metals into biomaterials such as spider silks and collagen membranes to improve their mechanical properties.[12] Furthermore, the Hupp group has employed VPI to modify metal nodes in NU1000, a MOF built with eight connected $Zr_6(\mu_3\text{-}O)_4(\mu_3\text{-}OH)_4(H_2O)_4(OH)_4$ nodes and 1,3,6,8-(*p*-benzoate)pyrene linkers, used for a variety of catalysis operations including water oxidation,[13] hydrogenation,[14] and oxidative dehydrogenation.[15] Although these previous results provide a fundamental understanding of gas phase metal–ligand coordination, none has successfully demonstrated a strain effect similar to what is presented here.

One of the most environmentally friendly approaches to achieve carbon-neutral energy conversion involves electrochemically converting CO_2 into chemical feedstock or fuel, such as carbon monoxide (CO). Thus far, extensive efforts have been devoted to the development of novel homogeneous and heterogeneous catalysts.[16] Nevertheless, outstanding challenges remain, such as improving the intrinsic activity of each catalytic site. Herein, we show that the internal strain induced by VPI can significantly improve catalyst activity. By using VPI to produce a Zn-porphyrin coordinated center on a surface-bound MOF followed by additional cycles of precursors, excess oxide growth within the MOF induced an internal stress, which deformed the Zn-porphyrin centers. Experimentally, the strained MOF demonstrated superior CO_2 reduction reactivity, selectivity, and durability compared to the unstrained MOF, the metal–ligand center of which was synthesized using the conventional solution-phase method.

Results and Discussion

MOF Synthesis and Vapor-Phase Infiltration

The MOF selected for this work was $Al_2(OH)_2TCPP\text{-}H_2$ [TCPP-H_2 = 4, 4′, 4″, 4‴-(porphyrin-5,10,15,20-tetrayl) tetrabenzonate], as this metalloporphyrin moiety is well acknowledged as a homogeneous electrocatalyst for CO_2 reduction to CO.[17] To grow a uniform MOF film on carbon fiber electrodes, a modified version of the strategy developed by Yang et al. was used.[16a] As illustrated in Figure 1, pristine MOF, $Al_2(OH)_2TCPP\text{-}H_2$, lacking Zn centers was synthesized by first depositing a thin layer of Al_2O_3 (10 nm) onto a carbon fiber electrode. Next, the oxide layer was reacted with tetrakis (4-carboxyphenyl) porphyrin (TCPP) in a microwave reactor to convert the oxide layer into a MOF. Afterwards, to synthesize the Zn-infiltrated sample (MOF-Zn-inf), gaseous diethylzinc and H_2O precursors were alternately introduced to the ALD chamber to coordinate with the nitrogen atoms on the porphyrin ring. Each deposition cycle consisted of six steps: diethyl zinc pulse (t_1), exposure (t_2), purge (t_3), H_2O pulse (t_4), exposure (t_5), and purge (t_6). Optimal infiltration times for each step were found to be: $t_1 = 0.05$ s, $t_2 = 60$ s, $t_3 = 60$ s, $t_4 = 0.05$ s, $t_5 = 60$ s, and $t_6 = 60$ s. For each infiltration cycle, diethyl zinc and H_2O were allowed enough time to diffuse into the pores and coordinate with the MOF. Thus, the

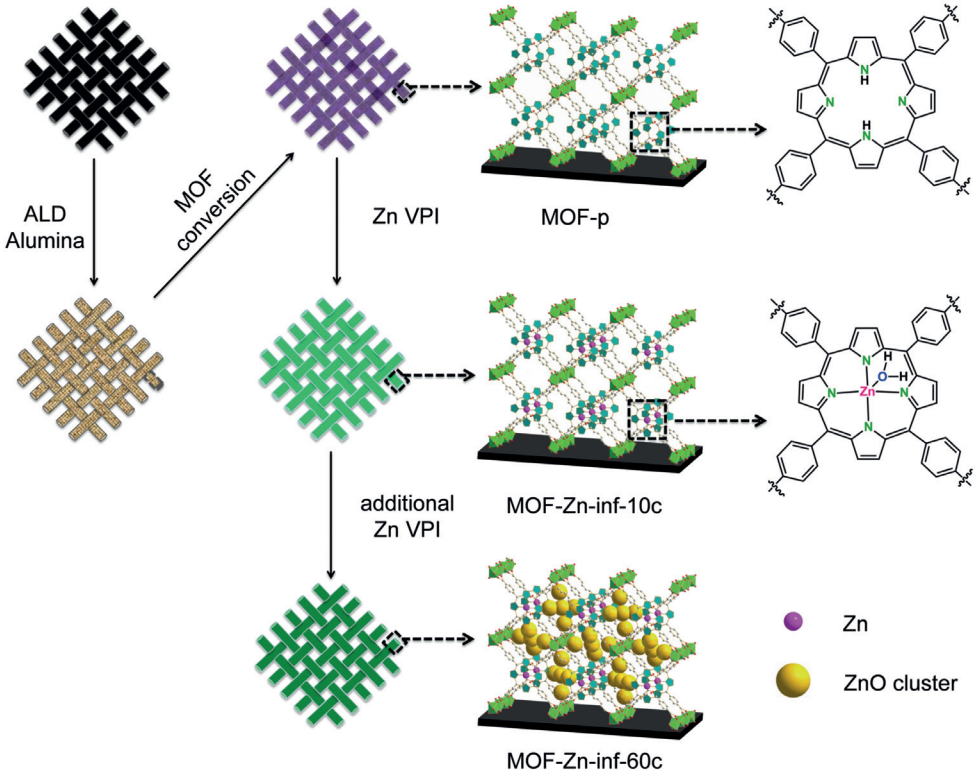

Figure 1. Illustration of the MOF template and vapor-phase infiltration. First, 10 nm of Al_2O_3 was deposited onto the carbon fiber electrode by ALD. Then, the deposited Al_2O_3 was reacted with TCPP to form MOF-p. Afterwards, the diethyl zinc and H_2O precursors were alternatively introduced to the porous MOF structure to coordinate with the porphyrin ($\leq$10 cycles). Finally, additional VPI cycles ($>$10 cycles) were run to form ZnO clusters inside the MOF pores and induce internal strain. Pink indicates Zn atoms occupying central MOF positions and yellow indicates ZnO clusters inside the MOF pores.

MOF fabricated by VPI is named Zn-MOF-inf, where inf refers to the infiltration process. Three control samples were studied in this work: 1) the pristine MOF, labeled MOF-p, 2) another MOF fabricated via the conventional solution metalation method, labeled MOF-Zn-s, and 3) a control sample, MOF-ZnO, that was synthesized without any exposure time for precursors to diffuse into the MOF channels ($t_2 = 0$ s and $t_5 = 0$ s). MOF-ZnO was thus formed with ZnO on top of the MOFs, similar to other prevailing ALD oxide thin film deposition procedures.[18] SEM images show the pristine MOF is composed of plate-like nanostructures (Supporting Information, Figure S1), with little change to the morphology after VPI.

Structure and Interface Characterization

To study the chemical environment and elemental distribution within MOF-Zn-inf and the other control samples, the interface of each sample was probed using scanning transmission electron microscopy (STEM) and energy dispersive X-ray spectroscopy (EDS). Figure 2a presents the cross-sectional STEM annular bright field (ABF) imaging of MOF-Zn-inf, where a MOF nanostructure with depth of 100–150 nm is observed. Cross-sectional EDS mapping (Figure 2b) shows a higher concentration of Al in the region closer to the Si surface, while Zn is distributed uniformly throughout the MOF interface (0–200 nm surface depth; Figure 2c). STEM-based EDS line profiling coupled with spectral component matching confirms a uniform distribution of Zn from the Si surface (depth = 0 nm) to the top of the MOF nanostructure (Figure 2d). N_2 adsorption analysis was also performed for the infiltrated MOF powder sample (Supporting Information, Figure S2), finding that the surface area of pristine MOF (873 $m^2 g^{-1}$) was decreased after 60-cycle infiltrating (MOF-Zn-inf-60c, 312 $m^2 g^{-1}$). Concurrently, the total micropore volume decreased from 0.34 $cm^3 g^{-1}$ to 0.14 $cm^3 g^{-1}$ comparing the pristine MOF to MOF-Zn-inf-60c (Supporting Information, Table S1); specifically, about 60% of the total micropore sites are occupied by ZnO after 60 cycles of infiltration, indicating successful penetration of the ZnO clusters into the porous structure of the MOF. In contrast, the Zn in MOF-ZnO is primarily distributed across the outermost surface of the MOF nanostructure, similar to traditional ALD deposition where the ALD layer is formed on top of the substrate (Figure 2g,h; Supporting Information, Figure S3e–h).[9b,19] This indicates that diffusion time is vital to the VPI process. If an insufficient amount of time is given for precursors to penetrate into the pores, ZnO clusters will form on the surface of the MOF structure. For comparison, Figure 2i–k depicts cross-sectional imaging and EDS chemical profiling of the solution-synthesized MOF-Zn-s, where the higher concentration of Zn is located at the bottom region of the MOF. This may correspond to elemental Al, thus the higher concentration of MOF, mainly accumulating at the bottom of the interface. Quantitatively, the atomic Zn concentration of MOF-Zn-s is much lower (ca. 0.1%) than that of the MOF-Zn-inf (ca. 0.6%-0.8%). These results support the VPI method's ability to form a homogeneous distribution of Zn sites within a nanoporous structure.

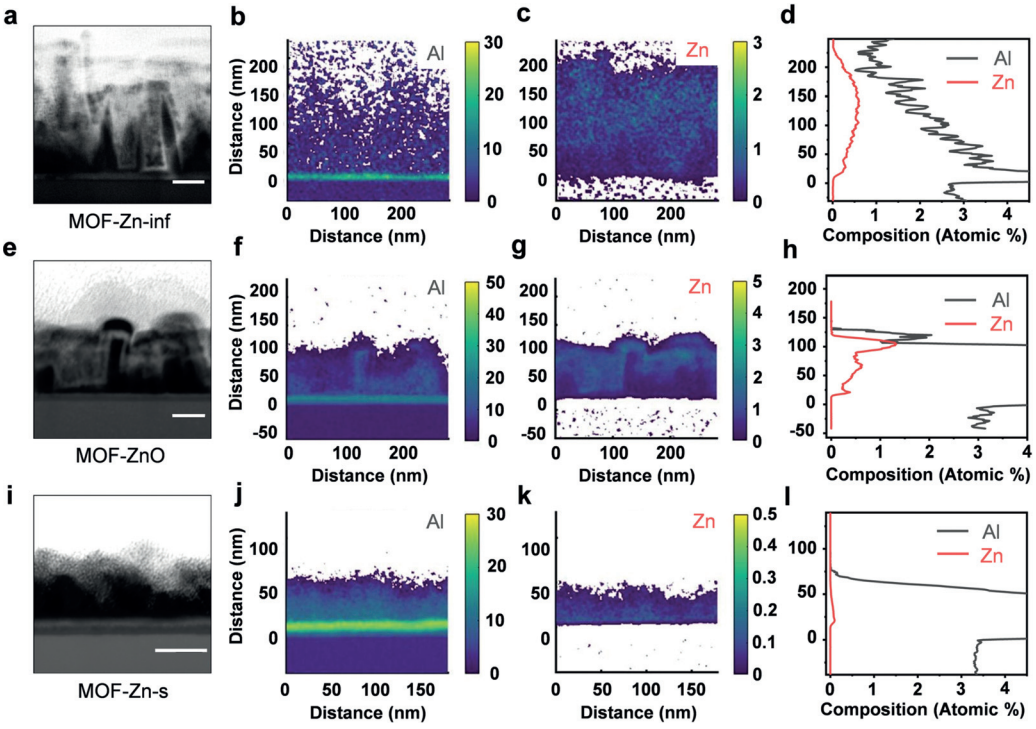

Figure 2. Structural characterization and chemical profiling. a),e),i) STEM images of MOF-Zn-inf, MOF-ZnO, and MOF-Zn-s. Scale bars: 50 nm. b),c),f),g),j),k) EDS mappings of Al and Zn. d),h),l) STEM EDS line profiling coupled with spectral components, atomic percentages, and elemental depth.

Crystallinity of MOF-p, MOF-Zn-s, MOF-Zn-inf, and MOF-ZnO on carbon fiber electrodes was characterized by X-ray diffraction (XRD) (Figure 3a; Supporting Information, Figure S4). MOF-p displayed XRD patterns similar to the theoretically simulated patterns,[16a,20] validating its structure. Retention of crystallinity in the two other control samples, MOF-Zn-s and MOF-ZnO, is demonstrated by the presence of a major characteristic diffraction peak at $2\theta = 7.6°$ corresponding to the formation of the (201) plane. Compared to other MOF analogues, however, the (201) characteristic reflection in the MOF-Zn-inf sample broadens and shifts to a lower degree at $2\theta = 7.4°$, indicating the generation of about 2.8% lattice strain. This conclusion is supported by the known effects of strain on both the position and width of diffraction peaks.[21] The broadening effect is an indication of nonuniform strain which causes bending or twisting of the MOF structure.[21] The strain is most likely induced by ZnO clusters grown inside the MOF structure during the VPI process, causing crystal lattice distortion similar to an overstuffed box. Existence of ZnO clusters is further confirmed by the presence of three additional characteristic peaks between 30° and 40° for both MOF-Zn-inf and MOF-ZnO, which correspond to the (100), (002), and (110) planes of ZnO.[22] Furthermore, the effect of varying the number of VPI cycles on internal strain was studied. XRD patterns (Figure 3b) show the (201) peak gradually shifts to a lower degree with increased VPI cycles (0–60 cycles), indicating a generation of about 1.0%, 1.6%, and 2.8% lattice strain on 20, 40, and 60 cycle samples, respectively. This data show VPI has the ability to generate fine-tuned internal strain. The featured peaks of ZnO remain at the same position during the VPI process, indicating that ZnO can act as an internal standard while demonstrating the gradual change in the MOF structure.

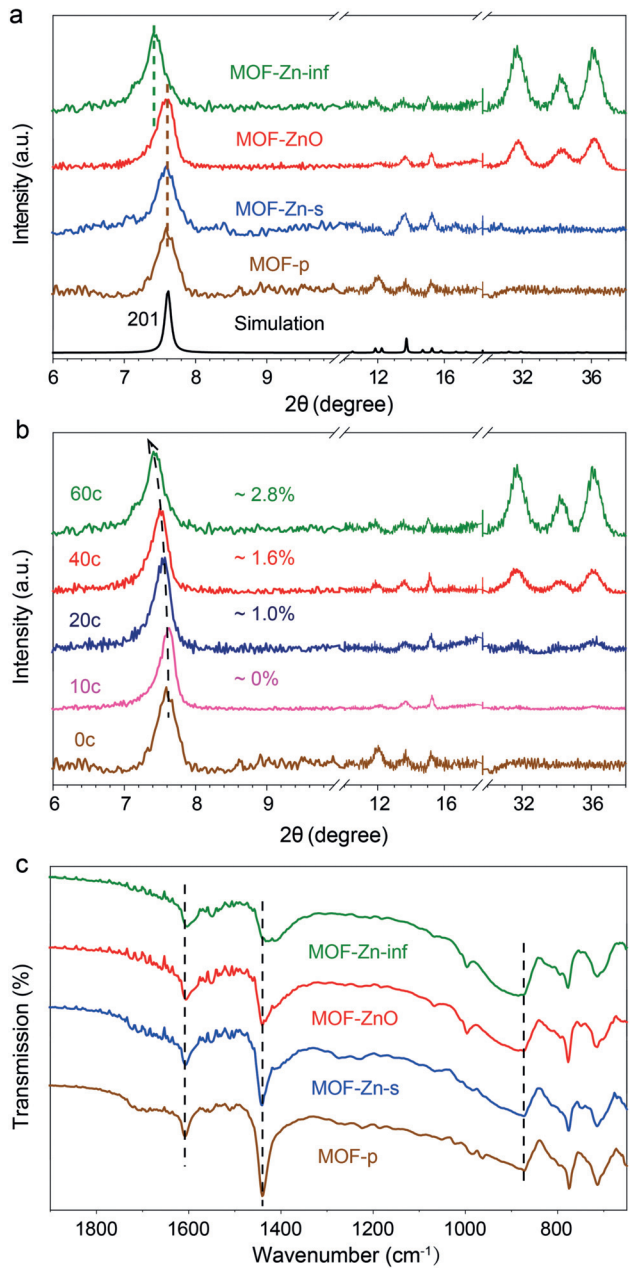

Figure 3. XRD and FTIR characterization. a) XRD of MOF samples on carbon fiber electrodes. b) XRD of VPI samples with various infiltration cycles. c) FTIR of MOF samples on Si substrates.

Fourier-transform infrared spectroscopy (FTIR) was also performed on all MOF compounds for additional structural characterization (Figure 3c). Similar broadening and shifting effects were observed for the infiltrated sample owing to tension prompted by the VPI process. The two strong carbonyl stretching peaks at 1610 cm^{-1} and 1450 cm^{-1} imply successful coordination of the carboxyl group with Al.[23] The other characteristic peaks of MOF-Zn-inf remain at the same vibration frequencies as those of MOF-p, indicating that the MOF template maintains the integrity of its organic-inorganic hybrid structure. Scanning electron microscopy (SEM) coupled with EDS also shows the MOF-Zn-inf sample consists of 3D plate-like nanostructures with uniform elemental distributions of Zn, Al, O, N, and C (Supporting Information, Figure S5).

Atomic and Electronic Structure Analysis

Synchrotron-based X-ray absorption spectroscopy (XAS) was employed to characterize the local coordination environment of MOF-Zn-inf and its analogues. Figure 4a compares the X-ray absorption near edge structure (XANES) spectra of MOF-ZnO, MOF-Zn-s, and MOF-Zn-inf synthesized with different numbers of VPI cycles. Interestingly, the XANES spectra of MOF-Zn-inf exhibit a gradual progression from a solution-like to a ZnO-like coordination environment as the number of infiltration cycles increases (Supporting Information, Figure S6). The XANES spectrum of MOF-Zn-inf-10c resembles that of solution-phase synthesized MOF-Zn-s, suggesting that the Zn center in the former adopts a similar electronic structure to the latter with Zn coordinated to the porphyrin ring. This agrees well with the XRD results in Figure 3b, where negligible ZnO was observed in the 10-cycle sample. In contrast, the XANES spectrum of MOF-Zn-inf-60c resembles that of MOF-ZnO and ZnO, implying that on the surface of MOF-Zn-inf-60c, the Zn center possesses local coordination environments similar to ZnO. Meanwhile, the XANES edge feature of MOF-Zn-inf-20c is positioned

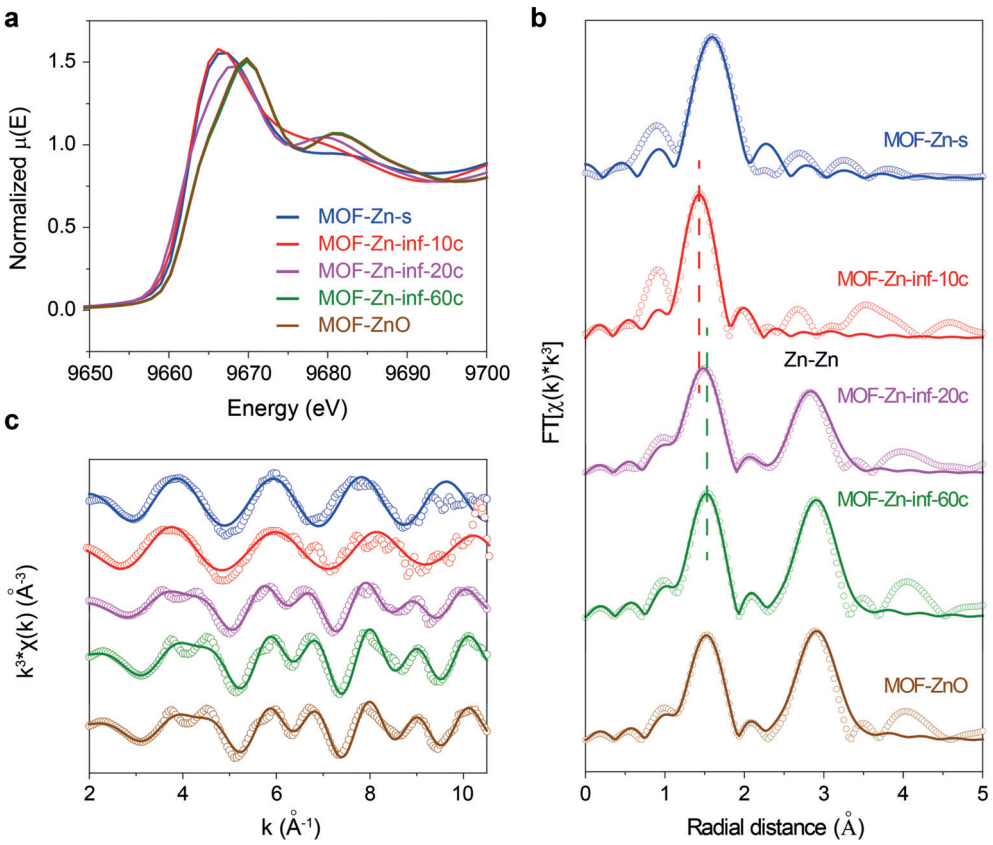

Figure 4. X-ray absorption analysis. a) Normalized Zn K-edge XANES spectra. b) Corresponding EXAFS spectra (○) and their fitting results (——) in R-space. Dashed lines indicate the peak position of Zn-ligand first shell for MOF-Zn-inf-10c and MOF-Zn-inf-60c. c) Corresponding EXAFS spectra (○) and their fitting results (——) in K-space.

between those of MOF-Zn-inf-10c and MOF-Zn-inf-60c, which implies the presence of Zn centers from both ZnO and Zn-N (the solution-phase analogue).

These results were further confirmed by extended X-ray absorption fine structure (EXAFS) spectroscopy (Figure 4b,c). In Figure 4b, the EXAFS spectra of MOF-Zninf-10c and MOF-Zn-s in R-space each feature one Zn-ligand first-shell peak, while an additional peak (attributed to a Zn-Zn path) was observed in the EXAFS spectra of MOF-Zninf-20c, MOF-Zninf-60c, and MOF-ZnO, where the amplitude of this Zn-Zn path is less intense in MOF-Zninf-20c. These results together indicate that Zn coordination strongly depends on the number of VPI cycles: more VPI cycles leads to a higher concentration of ZnO in the samples.

One explanation for the distinct XAS features is that the Zn precursor infiltrates into the MOF pores and metalates with the porphyrin when less than 10 VPI cycles are employed. However, when more than 20 cycles are employed in the VPI process, ZnO clusters form inside and on top of the MOF structure, which in turn contribute to the Zn–Zn peak. To gain further insight into the local geometry of the Zn center, EXAFS results were quantitatively analyzed using FEFF. The fitting model is shown in the Supporting Information, Figure S7 with the fitting results listed in Table S2. The Zn center in MOF-Zn-s is found to be coordinated to four N atoms with an average Zn–N distance of 2.08 Å, consistent with previous literature data.[24] As indicated by the similarity in the XANES spectra of MOF-Zn-s and MOF-Zn-inf-10c, it is expected that MOF-Zn-inf-10c will have the same Zn coordination geometry as MOF-Zn-s. Surprisingly, the EXAFS results of MOF-Zn-inf-10c cannot be adequately fitted unless an additional Zn–O path was added to form a five-coordinate square-pyramidal structure, where the four N atoms coordinate with the Zn atom on the macrocycle plane and the O atom coordinates to Zn perpendicular to the porphyrin plane (Figure 1). This Zn–O bond cannot be attributed to Zn–O–Zn bonds for the following reasons: 1) the Zn–Zn scattering path was not observed in XAS measurements, and 2) the Zn–O–Zn bond distance (ca. 7.2 Å) is much larger than the distance between two parallel porphyrin rings (6.6 Å) (Supporting Information, Figure S8), thus it cannot fit within the space provided. The spectrum with the best fit produces a Zn–O bond distance equal to 2.15 Å, which is similar to the Zn–O distance in five-coordinate Zn–OH_2.[25] Thus, we postulate that during the VPI process, H_2O precursors can weakly coordinate with the Zn center to form Zn–OH_2. For infiltrated MOF samples with VPI cycles ≥ 20, the EXAFS spectra can be fitted using the same model as ZnO. Results show similar Zn–O and Zn–Zn bond distances, suggesting that the Zn center in these samples is primarily coordinated to O atoms as Zn–O–Zn bonds on the surface.

Mechanistic Insight into the Effects of Strain Induction

To elucidate how the Zn precursor chemically interacts with the MOF substrate during the VPI process, UV/Vis absorption spectra of VPI conducted after various numbers of cycles were recorded (Figure 5a). The electronic absorption spectrum of the pristine MOF consists of two distinct regions, like typical porphyrins. The first region involves transition from the ground state to the second excited state and exhibits a corresponding Soret band at 407 nm. The second region exhibits a weak transition from the ground state to the first excited state, with four Q bands between 500–700 nm.[26] In the MOF-Zn-s sample, the red Soret band shifts to 416.7 nm

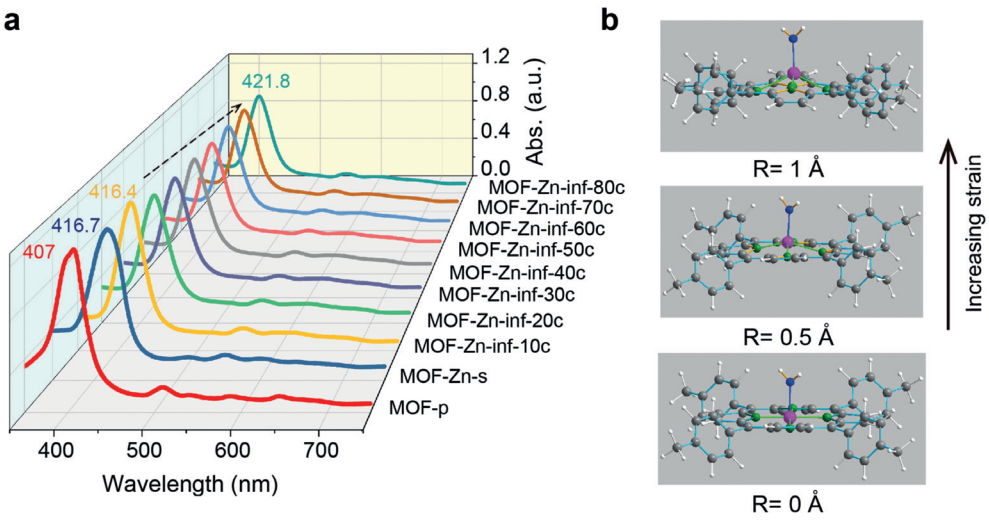

Figure 5. Impact of varied number of VPI cycles on MOF-Zn-inf. a) UV/Vis spectra of MOF-p, MOF-Zn-s, and MOF-Zn-inf with varied number of VPI cycles (0 to 80 cycles). b) DFT-predicted strain in MOF structures (Zn pink, C gray, N green, O blue, H white), correlated to UV/Vis changes provided in the Supporting Information, Table S3. Results demonstrate a gradual strain on the metal–ligand center.

after formation of the metalloporphyrin, implying successful Zn–N coordination, although a small tail from the strongest Q band around 530 nm still remains.[26] For the infiltration sample, after 10 VPI cycles (40 min), the Zn precursor fully coordinates with the ligand. The red Soret band shifts to 416.4 nm and the four Q bands evolve as two bands owing to the splitting of the pyrrole nitrogen atoms into two groups, similar to other metalloporphyrins.[26] The Zn porphyrin metalation was further confirmed by X-ray photoelectron spectroscopy (XPS). As shown in the Supporting Information, Figure S9, the high-resolution N 1s spectrum in the MOF-p contains two main peaks at 398.1 eV and 400.0 eV, corresponding to =N– and =NH–.[27] Introduction of Zn into the MOF, either by solution phase or VPI, evolves a new peak at 399.4 eV. This new peak is assigned to the formation of Zn–N coordinated bonds,[28] confirming that both the VPI and solution phase method successfully generates Zn–N coordinated bonds.

Interestingly, in the UV/Vis absorption spectra, as the number of ALD infiltration cycles increases from 10 to 80, the Soret and Q bands both gradually shift to longer wavelengths while decreasing in intensity. Comparing MOF-Zn-inf-10c to MOF-Zn-inf-80c, a shift from 416.4 nm to 421.8 nm is observed in the Soret band with a decrease in intensity of 16.8%. These results correlate well with the observed XRD peak shifts with various VPI cycles (Figure 3b). We postulate that changes in the absorption spectra are due to changes in internal strain experienced by the MOF. The shifts in UV spectra associated with the Soret and Q bands discontinue around 60 cycles, indicated by the lack of Soret and Q band peak shifting for MOF-Zn-inf-70c and MOF-Zn-inf-80c. This suggests that maximum internal strain was achieved at 60 cycles (MOF-Zn-inf-60c).

To support this hypothesis and shed light on this correlation, density functional theory (DFT) calculations were performed (Supporting Information, Table S3). Electronic transition wavelengths and intensities of the absorption spectra were calculated using a Zn metalloporphyrin molecule as a model, including a water molecule to maintain the five-fold coordination of the Zn. Assuming internal strain will cause a distortion of the Zn coordination sphere, we calculated the UV/Vis spectra for several fixed distances of the five-coordinate Zn from the center of the porphyrin ring. The geometry optimizes to a structure with coplanar nitrogen atoms and the Zn atom displaced 0.18 Å above the centroid of the N4 group. As the Zn atom is forced up or down along the axis perpendicular to and through the centroid of this plane, the N4 group becomes increasingly non-planar (see dihedral angles in the Supporting Information, Table S3). We parameterized this displacement as the distance R(Zn–N2) of the Zn center from the centroid of the pair of opposing porphyrin N atoms furthest from the water group (Figure 5b), and we varied that distance in increments of 0.25 Å from 0 (with the Zn colinear with one pair of N atoms) to 1.25 Å. The remaining geometrical parameters were optimized at each value of R(Zn–N2). The structural energies relative to the minimum energy, as well as the λ_{max} and peak intensity of the most intense feature in each of the predicted spectra, are listed in the Supporting Information, Table S3.

The DFT calculations demonstrate excellent correlation with changes in the observed UV/Vis spectra. As the Zn center distortion along the central axis increases from 0.18 Å to 1.25 Å, the simulated Soret bands gradually shift to the red (from 386 nm to 406 nm). At the same time, the maximum absorptivity is reduced from its initial value by about 20% (from 142 000 to 115 000 $L\,mol^{-1}\,cm^{-1}$). This simulation is a simplified model used to mimic the internal distortion inducing changes in structure. Even so, according to the XRD spectra, the distortion is nonuniformly induced throughout the entire MOF lattice. Therefore, it is difficult to simulate the exact distortion that occurs in the MOF-Zn-inf structures. Regardless, computed trends in the UV/Vis spectra demonstrate the great potential of the VPI technique for fine-tuning the degree of induced strain within porous material structures.

Evaluation of Carbon Dioxide Reduction Activity

Catalytic performance towards the electrochemical CO_2 reduction reaction (CO_2RR) was investigated in a CO_2-saturated solution (DMF/H_2O, v:v = 9:1). Initially, various MOF-Zn-inf samples with a range of applied VPI cycles were

compared to study the dependence of catalytic activity on internal strain. Four samples (20, 40, 60, and 80 cycles) were studied over the potential range of −1.0 V to −1.8 V vs. SHE. The 60-cycle sample (MOF-Zn-inf-60c) outperformed other infiltration samples with a maximum Faradaic efficiency (FE) of nearly 100% at −1.8 V (Supporting Information, Figure S10). Increasing the number of VPI cycles from 20 to 60, an increase in selectivity is observed. Additional cycles result in a circa 20–30% decrease in FE (80c), indicating that the added ZnO does not contribute to improvement of CO_2RR performance. This may be attributed to an excess of ZnO clusters forming on the outer surface, which then block the access of the reactants to the homogenous-like catalytic active sites. Similar FE observed for MOF-ZnO and MOF-Zn-inf-80c further supports this assumption (Supporting Information, Figure S11).

We postulate that the improved performance from 20 to 60 cycles for the infiltrated sample is related to the generation of the internal strain. During the VPI process, ZnO clusters fill the empty space of the MOF and induce gradual changes in internal tension. These internal changes alter the metal–porphyrin bond distance based on the DFT calculations, eventually improving the performance of the catalysts. As discussed previously, the parallel open space between the porphyrin rings is too confined for ZnO growth, therefore ZnO forms in the square-shaped regions (with size 11.6 Å × 11.6 Å) between the porphyrin and Al nodes (Supporting Information, Figure S8), where the empty space between porphyrin rings may facilitate the diffusion of reactants/products. The optimal catalytic activity was achieved at 60 cycles, agreeing well with UV/Vis absorption results which indicate that the maximized strain is also achieved at 60 cycles.

To further confirm the improved CO_2RR performance is correlated with internal strain, a MOF sample was prepared by first infiltrating with 10 VPI cycles to make Zn–N coordination bonds, then treating with 50 non-infiltration ALD cycles to form surface ZnO clusters without inducing internal strain (MOF-Zn-10c/ZnO-50c). This sample did not show superior performance over MOF-Zn-inf-10c (Supporting Information, Figure S12), suggesting that additional ZnO does not contribute to the CRR performance improvements. However, MOF-Zn-inf-60c demonstrated much higher performance, confirming that enhanced catalytic activity can be attributed to infiltration-induced strain rather than the catalytic performance induced by ZnO. Moreover, the 10-cycle infiltrated sample (MOF-inf-Zn-10c) showed similar performance compared to the solution synthesized sample (MOF-Zn-s), indicating that square pyramidal geometry and square planar Zn–N porphyrin catalytic centers have a similar catalytic effect (Supporting Information, Figure S13). To compare the CO_2 reduction activity of the strained (MOF-

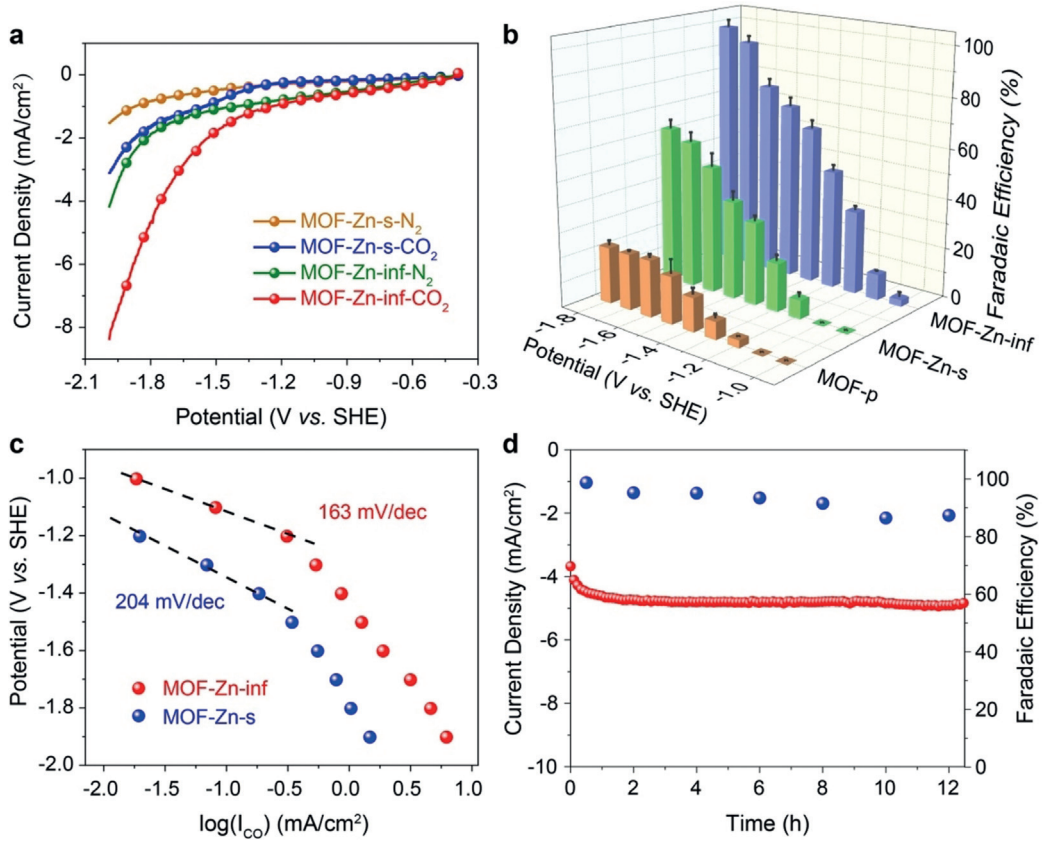

Figure 6. Catalytic performance and durability analysis. a) Polarization curves of MOF-Zn-inf-60c and MOF-Zn-s under N_2 and CO_2 saturated solutions (0.1 M tetrabutylammonium hexafluorophosphate in DMF/H_2O (v:v = 9:1)), respectively. b) Faradaic efficiencies of MOF-p, MOF-Zn-inf, and MOF-Zn-s at various applied potentials (−1.0 to −1.8 V vs. SHE). c) Corresponding Tafel plots of MOF-Zn-inf and MOF-Zn-s. d) Long-term durability test of MOF-Zn-inf at −1.8 V vs. SHE over 12 h.

Zn-inf-60c) and unstrained (MOF-Zn-s) catalysts, N_2 (or Ar) and CO_2 saturated linear sweep voltammetry (LSV) experiments were performed (Figure 6a; Supporting Information, Figure S14). Voltammogram traces of both samples unambiguously displayed great CO_2RR activity and noteworthy catalytic enhancement under the CO_2-saturated electrolyte, relative to the N_2- or Ar-saturated electrolyte. To understand the selectivity towards CO_2RR and reveal the nature of this catalytic process, the products were comprehensively analyzed using gas chromatography equipped with a barrier ionization discharge detector (GC-BID). Dramatic improvement in catalytic selectivity for CO_2RR was observed for MOF-Zn-inf compared to its analogue prepared in solution (Figure 6b). At a low overpotential (for example, −1.2 V vs. SHE), the FE of MOF-Zn-inf (FE ≈ 33 %) is approximately four times greater than solution-based MOF-Zn-s (FE ≈ 8 %). Meanwhile, at high overpotentials (−1.7 and −1.8 V vs. SHE), MOF-Zn-inf shows a conversion rate close to 100 % (98–100 %). This result is superior to MOF-Zn-s, whose FE reaches its limit at about 60 %. In the control experiment, the non-metalated MOF-p maximum selectivity is only 20 %. The onset potential of MOF-Zn-inf is −1.0 V vs. SHE, at least 200–300 mV more positive than that of its unstrained analogue, which is possibly due to a decrease in the activation barrier for the formation of absorbed COOH* intermediates.[29] A comparison of Tafel slopes between MOF-Zn-inf and MOF-Zn-s is provided in Figure 6c. The MOF-Zn-inf has a Tafel slope of 163 mV/decade, lower than the 204 mV/decade slope produced by MOF-Zn-s. These results imply that both metalated samples go through a one-electron reduction step to form a radical $CO_2^{\bullet-}$ as the rate-determining step in the overall catalytic process.[30] The durability of MOF-Zn-inf was studied for 12 h at −1.8 V vs. SHE in a CO_2-saturated solution. The current density during the potential-controlled electrolysis maintained its initial value with negligible degradation throughout the durability test (Figure 6d), while the CO selectivity only slightly decreased. Our post-electrolysis structural characterization results (Supporting Information, Figure S15) further confirm the longevity of the lattice-strained MOF. Comparison of the data collected in this experiment with applicable metalloporphyrins under non-aqueous solutions reported is provided in the Supporting Information, Table S5. Results reveal that the selectivity of MOF-Zn-inf is comparable to state-of-the-art molecular- and MOF-based catalysts for CO_2 reduction. In summary, with regard to experimental activity, selectivity, and stability data for CO_2RR, the MOF-Zn-inf sample outperforms the conventional MOF-Zn-s in all aspects.

Comparison of the VPI synthetic method proposed herein with traditional solution phase methods shows that the improvement of catalytic activity witnessed in porous material interfaces prepared by VPI is due to the creation of internally strained metal catalytic centers. Moreover, only 10 VPI cycles (40 min) are necessary to accomplish metal–ligand coordination, whereas the solution phase synthetic procedure is highly time-consuming (48 h). Furthermore, the VPI method is able to achieve better metal distributions across various depths due to how easily diffusion of small gas precursors through deep channels within porous materials occurs in this process. Finally, and most significantly, the ability to control the distribution of excess precursors by controlling the number of ALD cycles allows precise diffusion of the precursors into the channels of the porous structure, where they may react to form ZnO clusters and induce an internal strain within the MOF for further enhanced catalytic performance. Thus, while most strain studies to date have focused on surface strain,[2b,31] tunable internal strain stands to provide a powerful strategy to tailor the reactivity of metal–ligand catalytic sites.

Conclusion

High-efficiency, noble-metal-free strained Zn MOF-based electrocatalysts were developed by a facile and controllable VPI technique. Compared to previous studies of surface strain effects in heterogeneous catalysts, this work demonstrates the improved metalloporphyrin's intrinsic activity by fine-tuning internal strain on the Zn-porphyrin center. Using a MOF template to fix the ligand TCPP, followed by the VPI method to trigger the Zn-TCPP metalation and concurrently introduce ZnO clusters to create internal strain, the resulting catalytic performance for the MOF was significantly improved. The onset overpotential for the strained catalyst positively shifted by about 200 mV compared to the pristine MOF and conventional solution-based MOF-Zn-s. The Faradaic efficiency approached 100 % at −1.8 V, which is a circa 35–40 % increase compared to the solution-based MOF-Zn-s and 40–75 % increase compared to the pristine MOF. Mechanistic studies which employ XAS, STEM, UV/Vis, and DFT calculations reveal that internal strain can be precisely controlled by the number of ALD cycles applied and is correlated to the UV/Vis spectral changes. XAS displayed square pyramidal coordination of the gas-phase synthesized metal center, with four Zn–N bonds and one Zn-OH_2 bond. The method of combining vapor phase infiltration to create elastic strain internally in a porous structure can be a general technique used to improve the catalytic activity of many porous materials. Thus, this report presents groundwork for universal application of the VPI technique for reactions beyond CO_2RR and for materials beyond $Al_2(OH)_2$TCPP MOF.

Acknowledgements

F.Y., J.G., M.P. acknowledge San Diego State University (SDSU) start-up funds and National Science Foundation (CBET-1704992) to support this research. J.H. and W.H. acknowledges the support from National Science Foundation (DMR-1654140) and ACS-PRF (57503-DNI6). Use of the Advanced Photon Source at Argonne National Laboratory was supported by the U.S. Department of Energy, Office of Science, Office of Basic Energy Sciences, under Award No. DE-AC02-06CH11357. Work at the Molecular Foundry was supported by the Office of Science, Office of Basic Energy Sciences, of the U.S. Department of Energy under Contract

No. DE-AC02-05CH11231. Y.Z. acknowledges National Natural Science Foundation of China (No.21771004).

[1] A. Khorshidi, J. Violet, J. Hashemi, A. A. Peterson, *Nat. Catal.* **2018**, *1*, 263.

[2] a) W. Cheng, X. Zhao, H. Su, F. Tang, W. Che, H. Zhang, Q. Liu, *Nat. Energy* **2019**, *4*, 115; b) M. Luo, S. Guo, *Nat. Rev. Mater.* **2017**, *2*, 17059.

[3] D. V. Potapenko, Z. Li, J. W. Kysar, R. M. Osgood, *Nano Lett.* **2014**, *14*, 6185 – 6189.

[4] A. Castellanos-Gomez, R. Roldán, E. Cappelluti, M. Buscema, F. Guinea, H. S. van der Zant, G. A. Steele, *Nano Lett.* **2013**, *13*, 5361 – 5366.

[5] H. Wang, S. Xu, C. Tsai, Y. Li, C. Liu, J. Zhao, Y. Liu, H. Yuan, F. Abild-Pedersen, F. B. Prinz, *Science* **2016**, *354*, 1031 – 1036.

[6] a) C. He, D. Liu, W. Lin, *Chem. Rev.* **2015**, *115*, 11079 – 11108; b) A. Kirchon, L. Feng, H. F. Drake, E. A. Joseph, H.-C. Zhou, *Chem. Soc. Rev.* **2018**, *47*, 8611 – 8638.

[7] T. Zhang, W. Lin, *Chem. Soc. Rev.* **2014**, *43*, 5982 – 5993.

[8] K. J. Gagnon, C. M. Beavers, A. Clearfield, *J. Am. Chem. Soc.* **2013**, *135*, 1252 – 1255.

[9] a) J. Gu, Y. Yan, J. L. Young, K. X. Steirer, N. R. Neale, J. A. Turner, *Nat. Mater.* **2016**, *15*, 456; b) J. Gu, J. A. Aguiar, S. Ferrere, K. X. Steirer, Y. Yan, C. Xiao, J. L. Young, M. Al-Jassim, N. R. Neale, J. A. Turner, *Nat. Energy* **2017**, *2*, 16192; c) S. Hu, M. R. Shaner, J. A. Beardslee, M. Lichterman, B. S. Brunschwig, N. S. Lewis, *Science* **2014**, *344*, 1005 – 1009.

[10] C. Z. Leng, M. D. Losego, *Mater. Horiz.* **2017**, *4*, 747 – 771.

[11] a) L. Zhang, A. J. Patil, L. Li, A. Schierhorn, S. Mann, U. Gösele, M. Knez, *Angew. Chem. Int. Ed.* **2009**, *48*, 4982 – 4985; *Angew. Chem.* **2009**, *121*, 5082 – 5085; b) J. R. Avila, J. D. Emery, M. J. Pellin, A. B. Martinson, O. K. Farha, J. T. Hupp, *ACS Appl. Mater. Interfaces* **2016**, *8*, 19853 – 19859.

[12] a) S. M. Lee, E. Pippel, M. Knez, *ChemPhysChem* **2011**, *12*, 791 – 798; b) S.-M. Lee, E. Pippel, U. Gösele, C. Dresbach, Y. Qin, C. V. Chandran, T. Bräuniger, G. Hause, M. Knez, *Science* **2009**, *324*, 488 – 492.

[13] C.-W. Kung, J. E. Mondloch, T. C. Wang, W. Bury, W. Hoffeditz, B. M. Klahr, R. C. Klet, M. J. Pellin, O. K. Farha, J. T. Hupp, *ACS Appl. Mater. Interfaces* **2015**, *7*, 28223 – 28230.

[14] P. Ji, K. Manna, Z. Lin, A. Urban, F. X. Greene, G. Lan, W. Lin, *J. Am. Chem. Soc.* **2016**, *138*, 12234 – 12242.

[15] Z. Li, A. W. Peters, V. Bernales, M. A. Ortuño, N. M. Schweitzer, M. R. DeStefano, L. C. Gallington, A. E. Platero-Prats, K. W. Chapman, C. J. Cramer, *ACS Cent. Sci.* **2017**, *3*, 31 – 38.

[16] a) N. Kornienko, Y. Zhao, C. S. Kley, C. Zhu, D. Kim, S. Lin, C. J. Chang, O. M. Yaghi, P. Yang, *J. Am. Chem. Soc.* **2015**, *137*, 14129 – 14135; b) C. Wang, Z. Xie, K. E. deKrafft, W. Lin, *J. Am. Chem. Soc.* **2011**, *133*, 13445 – 13454; c) K. A. Grice, *Coord. Chem. Rev.* **2017**, *336*, 78 – 95.

[17] a) C. Costentin, S. Drouet, M. Robert, J.-M. Savéant, *Science* **2012**, *338*, 90 – 94; b) Y. Wu, J. Jiang, Z. Weng, M. Wang, D. L. Broere, Y. Zhong, G. W. Brudvig, Z. Feng, H. Wang, *ACS Cent. Sci.* **2017**, *3*, 847 – 852; c) A. J. Morris, G. J. Meyer, E. Fujita, *Acc. Chem. Res.* **2009**, *42*, 1983 – 1994.

[18] A. Loiudice, S. Saris, E. Oveisi, D. T. Alexander, R. Buonsanti, *Angew. Chem. Int. Ed.* **2017**, *56*, 10696 – 10701; *Angew. Chem.* **2017**, *129*, 10836 – 10841.

[19] M. T. McDowell, M. F. Lichterman, A. I. Carim, R. Liu, S. Hu, B. S. Brunschwig, N. S. Lewis, *ACS Appl. Mater. Interfaces* **2015**, *7*, 15189 – 15199.

[20] Y. Zhao, N. Kornienko, Z. Liu, C. Zhu, S. Asahina, T.-R. Kuo, W. Bao, C. Xie, A. Hexemer, O. Terasaki, *J. Am. Chem. Soc.* **2015**, *137*, 2199 – 2202.

[21] a) B. Nasiri-Tabrizi, *J. Adv. Ceram.* **2014**, *3*, 31 – 42; b) P. Cendula, A. Malachias, C. Deneke, S. Kiravittaya, O. G. Schmidt, *Nanoscale* **2014**, *6*, 14326 – 14335.

[22] M. R. Arefi, S. Rezaei-Zarchi, *Int. J. Mol. Sci.* **2012**, *13*, 4340 – 4350.

[23] R. Rahimi, S. Shariatinia, S. Zargari, M. Y. Berijani, A. Ghaffarinejad, Z. S. Shojaie, *RSC Adv.* **2015**, *5*, 46624 – 46631.

[24] S. Lipstman, I. Goldberg, *Beilstein J. Org. Chem.* **2009**, *5*, 77.

[25] H. Song, C. A. Reed, W. R. Scheidt, *J. Am. Chem. Soc.* **1989**, *111*, 6867 – 6868.

[26] R. Giovannetti, *Macro to nano spectroscopy*, IntechOpen, **2012**.

[27] M. Nardi, R. Verucchi, C. Corradi, M. Pola, M. Casarin, A. Vittadini, S. Iannotta, *Phys. Chem. Chem. Phys.* **2010**, *12*, 871 – 880.

[28] a) K. Diller, A. C. Papageorgiou, F. Klappenberger, F. Allegretti, J. V. Barth, W. Auwärter, *Chem. Soc. Rev.* **2016**, *45*, 1629 – 1656; b) V. N. Nemykin, P. Galloni, B. Floris, C. D. Barrett, R. G. Hadt, R. I. Subbotin, A. G. Marrani, R. Zanoni, N. M. Loim, *Dalton Trans.* **2008**, 4233 – 4246; c) T. E. Shubina, H. Marbach, K. Flechtner, A. Kretschmann, N. Jux, F. Buchner, H.-P. Steinrück, T. Clark, J. M. Gottfried, *J. Am. Chem. Soc.* **2007**, *129*, 9476 – 9483.

[29] F. Pan, H. Zhang, K. Liu, D. Cullen, K. More, M. Wang, Z. Feng, G. Wang, G. Wu, Y. Li, *ACS Catal.* **2018**, *8*, 3116 – 3122.

[30] a) P. Russell, N. Kovac, S. Srinivasan, M. Steinberg, *J. Electrochem. Soc.* **1977**, *124*, 1329 – 1338; b) T. Hatsukade, K. P. Kuhl, E. R. Cave, D. N. Abram, T. F. Jaramillo, *Phys. Chem. Chem. Phys.* **2014**, *16*, 13814 – 13819.

[31] a) L. Wang, Z. Zeng, W. Gao, T. Maxson, D. Raciti, M. Giroux, X. Pan, C. Wang, J. Greeley, *Science* **2019**, *363*, 870 – 874; b) J. R. Kitchin, J. K. Nørskov, M. A. Barteau, J. Chen, *Phys. Rev. Lett.* **2004**, *93*, 156801.